



Effect of Deposition Strategies on the Microstructure and Tensile Properties of Wire Arc Additive Manufactured Al-5Si Alloys

Chuanchu Su, Xizhang Chen, Sergey Konovalov, R. Arvind Singh, S. Jayalakshmi, and Lei Huang

Submitted: 2 September 2020 / Revised: 15 January 2021 / Accepted: 23 January 2021 / Published online: 16 February 2021

4043 Al-5Si alloy components were fabricated by wire and arc additive manufacturing based on cold metal transfer (WAAM-CMT). Three deposition strategies, i.e. the method of building the layers and tracks (Line 90°, Cycle line 90°, and Line 45°), were employed during the process, and their impact on the microstructure and tensile properties of the deposited Al-5Si alloy was evaluated. Results showed that the samples with different deposition strategies exhibited similar phase composition (α -Al, Si phase, and Al₃Si phase), but various deposited layer size, grain size, and Si morphology owing to different deposition strategies. Recrystallization was observed in all deposition processes. The average micro-hardness was ~ 52.3 Hv, yield strength (YS) varied between 130 and 150 MPa, ultimate tensile strength (UTS) changed between 200 and 230 MPa and elongation (EL) ranged between 10 and 12%. Based on the fractographic analysis, the fracture mechanism was identified to be due to the presence of numbers of sharp-angled defects like cracks and chain-like micro-pores.

Keywords Al-5Si alloy, deposition strategies, microstructure, tensile properties, WAAM-CMT

1. Introduction

Aluminum alloys have been widely used as materials in aerospace, automotive and marine applications owing to their lightweight, high specific strength, specific modulus, wear resistance, and excellent corrosion resistance, among which Al-Si alloys occupy the vast majority of application market in industrial applications comparing to other series of aluminum alloys (Ref 1, 2). In recent years, they have gained much attention to be produced by additive manufacturing (AM) process (Ref 3, 4) due to their good thermal conductivity, low tendency to produce cracks, and better castability/weldability.

Among all AM processes, wire and arc additive manufacture (WAAM) based on cold metal transfer (CMT) provides a promising method for rapidly manufacturing Al-Si alloys with low heat input and large geometries, at low cost (Ref 5). For the WAAM-CMT Al-Si alloys process, it is evident that a correct understanding of WAAM-CMT deposition and parts processing is necessary, in order to control the deposition quality and performance of parts. Chen et al. (Ref 6) had proved that the manufacturing system using WAAM-CMT technology had

stability and reliability of Al-5Si parts deposition, and they reported that this technology possesses the characteristics of no spatter, good AM ability and low thermal input based on a specific short-circuiting transfer process. Yang et al. (Ref 7) studied the effect of heat treatment on the elemental distribution, microstructure and mechanical properties of WAAM-CMT AlSi7Mg0.6 alloy. It was noted that the shape change of Si phase and precipitation strengthening improved the strength with no reduction in ductility. Ortega et al. (Ref 8) investigated the transfer mechanisms and geometrical characteristics of the Al-5Si alloy deposits using the CMT process as well as improved the geometrical accuracy of parts by better controlling the main process parameters such as travel speed and wire feeding speed. The deposition strategy as one of the process parameters is also considered to play an important role during the WAAM process. Several studies have been focused on analyzing the impact of the laser deposition strategy on the processing of metals and alloys (i.e. in selective laser melting (SLM)). For example, Larrosa et al. (Ref 9) investigated the effect of build orientation by 90° rotation of consecutive layers on the porosity of SLM AlSi10Mg samples, while Zhang et al. (Ref 10) reported the effect of changing scanning strategy to decrease defects (pores) and improve mechanical properties in AlSi10Mg parts. Liu et al. (Ref 11) showed that rotations of 67° during SLM AlSi10Mg deposition process resulted in equiaxed and columnar grains, and a higher cooling rate promoted the formation of equiaxed grains. Similar research by Kimura et al. (Ref 12) in AlSi7Mg0.3 samples showed fine dendritic cell microstructures and superior mechanical properties. Guan et al. (Ref 13) found microstructural evolution and texture orientation of AlSi10Mg samples were influenced by the scanning strategy of SLM. Prashanth et al. (Ref 14) showed that varying scanning strategies had a crucial impact on texture and the crack propagation mechanism in the Al-12Si sample. From these research works, it could be seen that the effect of deposition strategy on WAAM-CMT deposited aluminum alloys has not been researched yet and it is necessary to study the microstruc-

Chuanchu Su, Xizhang Chen, Sergey Konovalov, and Lei Huang, College of Mechanical and Electrical Engineering, Wenzhou University, Chashan Education Town, Wenzhou 325035 Zhejiang, China; and Department of Metals Technology and Aviation Materials, Samara National Research University, 34, Moskovskoye Shosse, Samara, Samara, Russia 443086; and **R. Arvind Singh and S. Jayalakshmi,** College of Mechanical and Electrical Engineering, Wenzhou University, Chashan Education Town, Wenzhou 325035 Zhejiang, China. Contact e-mail: Kernel.chen@gmail.com.

tures and mechanical properties of aluminum alloys under various deposition strategy, considering that the WAAM-CMT is a very promising AM process.

In this work, three different deposition strategies (i.e. the trajectory of building the layers and tracks) have been employed to WAAM-CMT Al-5Si alloys. And the effect of microstructural characteristics on the variation of mechanical properties of the samples and tensile fracture mechanism has been investigated.

2. Materials and Methods

2.1 Materials

In this study, commercial Al-5Si alloy filler wire (FW) with a diameter of 1.2 mm was selected as the deposition material. And 6061-T6 aluminum alloy plate with a dimension of 200 mm×60 mm×10 mm was mechanically cleaned and fixed on the workbench before the manufacturing process and was employed as the base metal (BM). The nominal chemical composition of BM and FW is listed in Table 1.

2.2 WAAM-CMT of Samples

The multi-track multi-layer Al-5Si alloy walls with a dimension of 150 mm × 70 mm × 32 mm were deposited by WAAM-CMT system equipped with 3D path simulation software (DingzhiPNT), Fronius CMT-Advance power source, 6-axis FANUC robot, wire feeder, Ar gas and a robot controller. To obtain sound deposited samples avoiding defects, the optimized parameters (e.g., wire feed speed, arc current, arc voltage, and deposition speed) for the deposition of the material were selected, which are listed in Table 2. Among parameters,

Table 1 Chemical composition of the filler wire and base metal (wt.%)

Composition	Si	Fe	Cu	Mn	Mg	Al
4043 (FW)	4.5–6.0	0.8	0.3	0.05	0.05	Balance
6061 (BM)	0.4–0.8	0.7	0.15–0.4	0.15	0.8–1.2	Balance

Table 2 WAAM-CMT processing parameters

Parameter	Value/unit
Current	113A
Voltage	11.2V
Deposition speed	0.6 m/min
Wire feeding speed	5.5m/min
Filler wire	ER4043
Wire diameter	1.2mm
Shielding gas	Ar
Ar flow rate	25L/min
CMT mode	CMT
Weld overlap rate	25%

the weld overlap rate represented the repeat ratio of overlap with the value of 25% between multi-tracks. And three types of deposition strategies with a rotation between the successive layers were adopted to produce the Al-5Si alloy samples. As shown in Fig. 1, the x -axis direction is along the deposition direction (D_x), the y -axis is along the transverse direction (D_y), and the z -axis is along the vertical direction (D_z). The deposition strategy Line 90° was deposited with a rotation of 90° in successive layers, while 45° rotation was used in deposition strategy Line 45°. The deposition strategy Cycle line 90° (CL 90°) possessed the paths in the clockwise direction among the deposition layers.

2.3 Samples Machining and Analysis

The cross section of the bulk alloy (sample E) for metallographic analysis was ground, polished (the samples were mounted in a resin), and etched with Keller's solution for about 15 seconds. The 3D measuring laser microscope (OLYMPUS- OLS40-CB) with calculated software was used to test the center bead width and height of the sample with 10 times measures, respectively, as well as the microstructure and secondary dendrite arm spacing (SDAS) or the length of cellular grains of the whole sample in each alloy. Due to the three different deposited strategies, the difference in grain size and mechanical properties of the as-deposited samples can result. The cooling rate analysis of the samples prepared by the three-deposition strategies was conducted via measurement of secondary dendrite arm spacing (SDAS) or the length of cellular grains [measured as (Ref 7)]. The average length size (L_{ave}) was subsequently calculated using Eq 1 and a characteristic cooling rate could be expressed with the empirical formula (Eq 2). Equation 1 and 2 are mentioned below:

$$L_{ave} = \frac{L_S N_C + L_C N_S}{2N_C N_S} \quad (\text{Eq 1})$$

$$CR = \left(\frac{L_{ave}}{B} \right)^{-1/n} \quad (\text{Eq 2})$$

where L_S is the length in μm and N_S is the number of dendrite arm spaces, L_C is the length of cellular grains and N_C is the number of cellular grains, CR is the cooling rate (Ks^{-1}) and for Al-5Si, the constants of B and n were $50 \text{ mm} (\text{Ks}^{-1})^n$ and 0.33 (Ref 15, 16), respectively, which were determined by material and process.

The deposited building planes of samples were subjected to x-ray diffraction (XRD) for phase identification and crystallographic preferential orientation analysis (Bruker D8 ADVANCE automatic diffractometer with Cu target $K\alpha$ radiation). Electron backscatter diffraction (EBSD) test with a scan step size of 1.2 μm was performed to obtain total grain size in the deposited layers. Vickers micro-hardness tests were performed at the mid-height and along the mid-width direction of samples, with 200 g force and an indentation dwells time of 10 s at a periodic gap of 1 mm. Ten standard round tensile bars were machined from blocks of each sample alloy. Five tensile bars were oriented parallel (D_x) to the O_X direction (as shown in Fig. 2) and five tensile bars were oriented perpendicular (D_y) to it in as-deposited layers to evaluate mechanical performance. Tensile tests were conducted in an automated mechanical universal tensile machine (Hualong WDW-100) using a 22 kN

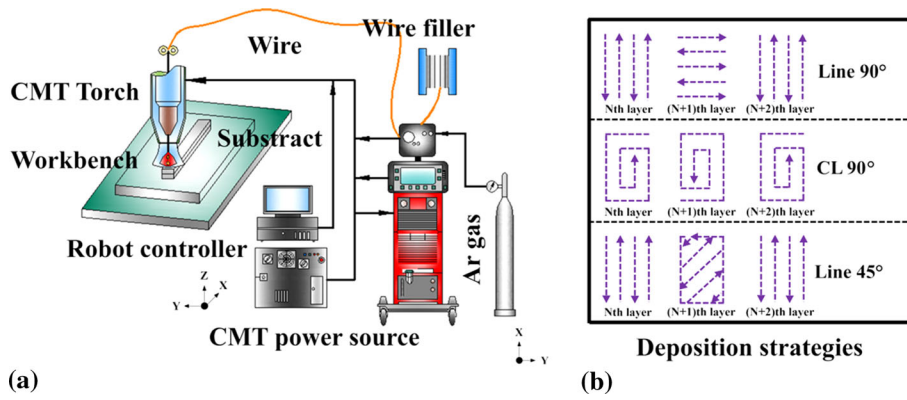


Fig. 1 (a) The schematic process of WAAM-CMT, (b) as-used deposition strategies: Line 90°: deposition with a rotation of 90° in successive layers, CL 90°: paths in the clockwise direction among the deposition layers and Line 45°: deposition with a rotation of 45° in successive layers

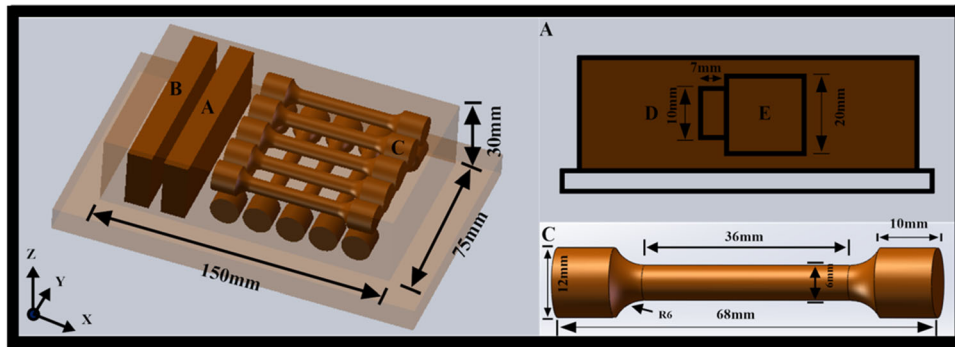


Fig. 2 Schematic diagram of samples used for the tests: (a) A-a sample used for micromorphology observation, B-a sample taken for macro-morphology observation and the measurement of micro-hardness, (b) C-a sample used for tensile sample dimension, D-a sample taken for XRD and EBSD tests and E-a sample used for macroscopic size and microstructure observation

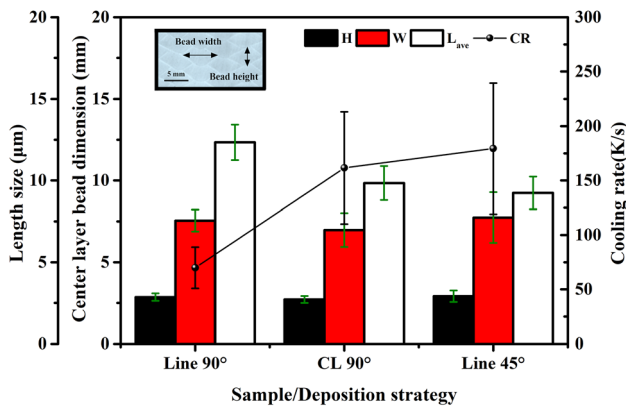


Fig. 3 Average center layer bead dimension (H-bead height, W-bead width: mm), average length size (L_{ave} : μm), and cooling rate (CR: k/s) for Al-5Si alloys with corresponding deposition strategy

load cell at a loading rate of 2.0 mm/min. Phenom-XL scanning electron microscopy (SEM) with energy-dispersive spectroscopy (EDS) was used to observe the fractured samples and test the chemical composition of fractures.

3. Results and Discussion

3.1 Deposited Dimension of Three-Strategies Samples

The measurement of the deposited layer size fabricated using different deposition strategies is shown in Fig. 3, the average value of center layer bead width ranges from approximately 6.97 to 7.55 mm, but the dimension of center layer bead height is a little different. The samples in Line 90° process exhibit the largest center layer bead widths and are statistically equivalent.

3.2 XRD of WAAM-CMT Samples

Based on the XRD data presented in Fig. 4, the main phase in WAAM-CMT samples with different deposition strategies is α -Al, Si phase, and the intermetallic phase Al_3Si (Ref 17). New diffraction peaks belonging to other phases (other than the ones mentioned above) are not detected after depositing with different deposition strategies, indicating that phase transformations do not occur during the WAAM-CMT process. Moreover, clear differences among the three states could be seen in the α -Al phase. There is a fairly strong peak of the main (111) crystallographic orientation in all the samples, the peak intensity of which increases when the deposition strategy

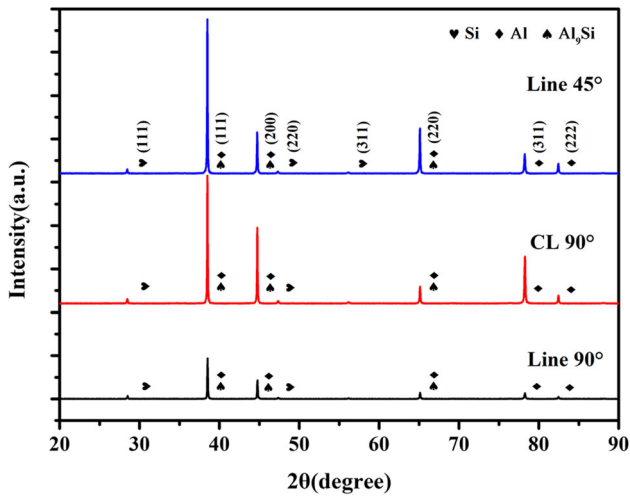


Fig. 4 XRD of WAAM-CMT Al-5Si alloys

changes from Line 45° process to Line 90° process, though the sample orientations of CL 90° process have preferential growth along the (200) plane for the Al phase. The small variations of other α -Al phase intensity indicate the percentage of this particular orientation varies from one to the other, which ascribe to the change of deposition strategies. It is concluded that the rotation of the lattice plane in samples is influenced by the deposition strategies.

3.3 Microstructure

It is known that the most important solidification variables are thermal gradient (G) and solidification rate (R). Moreover, $G \times R$ (representing cooling rate) determines the fineness of the microstructure, where with the increase in $G \times R$, finer structures are expected to form in sequence (Ref 18, 19). The WAAM-CMT is a heat accumulation process, the samples of which consist of regions of inner-layers and inter-layers. By comparing with the uniform microstructures of the inner-layer regions among different deposition strategies (Fig. 5), the mostly

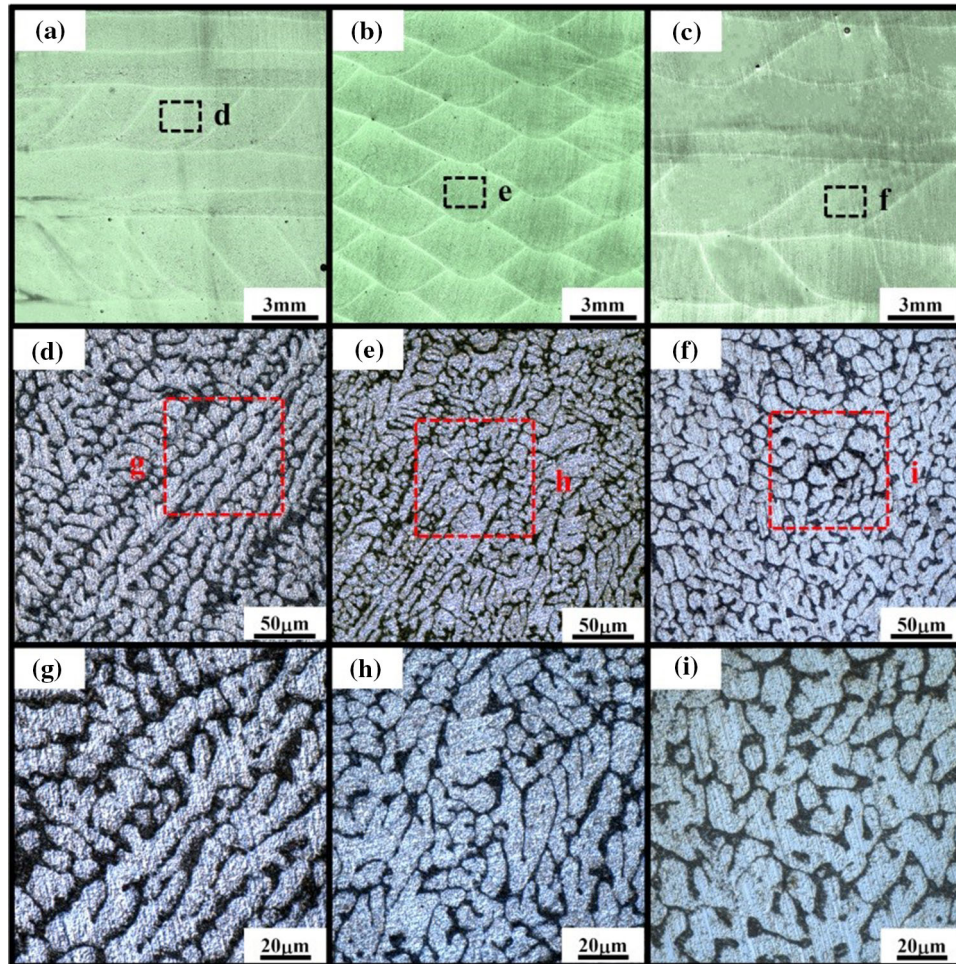


Fig. 5 Cross-section macrograph and micrograph of Al-5Si under different deposition strategies: (a, d, g) Line 90°, (b, e, h) CL 90°, (c, f, i) Line 45°

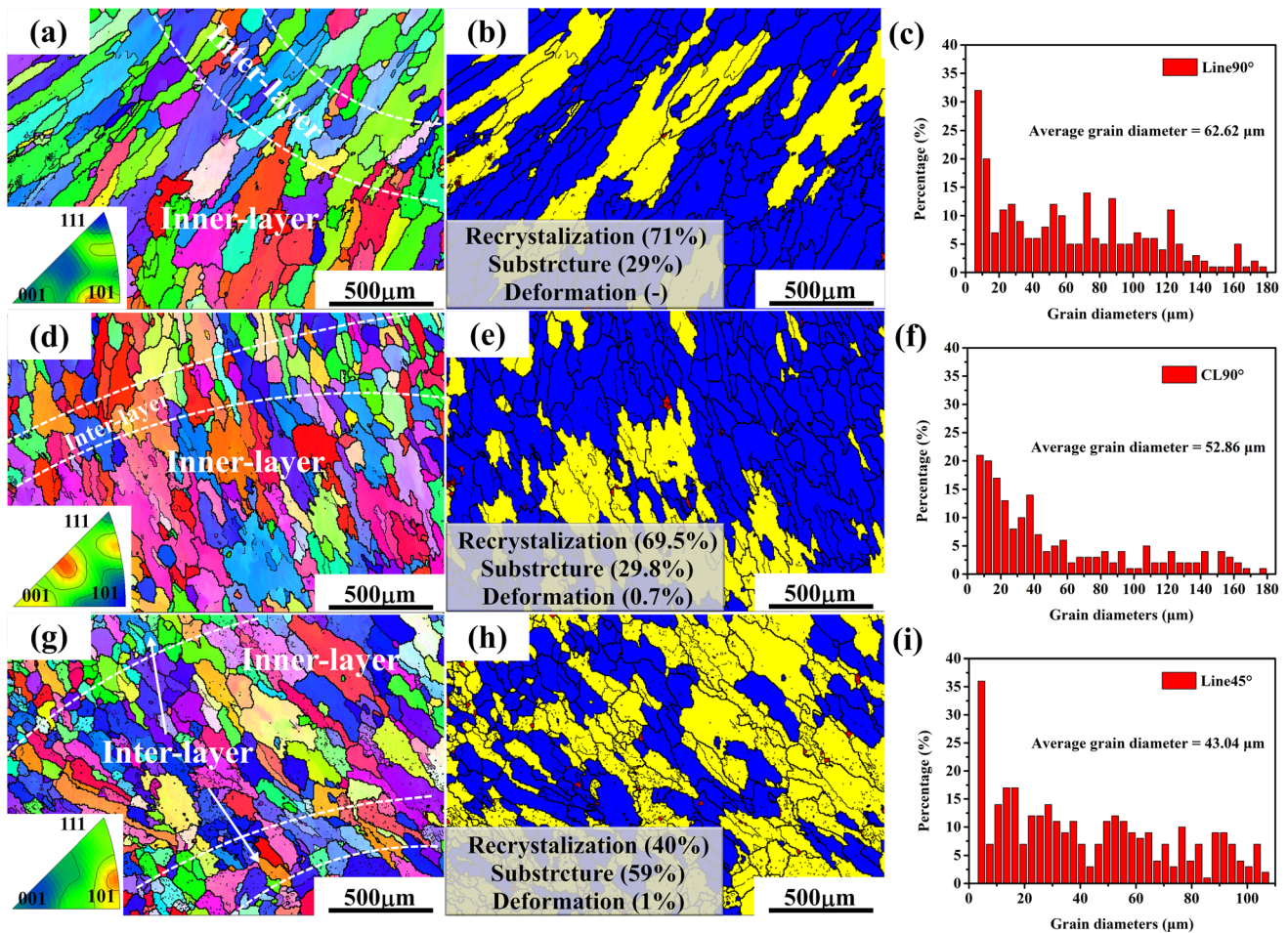


Fig. 6 The EBSD analysis of microstructure and grain size distribution of WAAM-CMT Al-5Si alloys: (a, b, c) Line 90°, (d, e, f) CL 90°, (g, h, i) Line 45°

columnar/columnar dendritic and a few of equiaxed morphology were exhibited in samples, and the microstructure is distinct and inhomogeneous. In Line 45° process, the α -Al phase mainly tends to be more equiaxed and the Si phase is distributed along grain boundaries with a fibrous morphology, while some dendritic structure remains in microstructure. In Line 90° process, the Si phase modifies into mostly needle-like or rod-like shape. Simultaneously, the condition of the CL 90° process presents an intermediate structure (Ref 20, 21). Besides, there is a relatively division between the different length sizes in secondary dendrite arm spacing or cellular grains among three different deposition strategies. The quantitative statistics results of dendrite arm spacing or cellular grain are shown in Fig. 3, which shows that the average length size of the samples is about 12.34 μm in Line 90° process, 9.84 μm in CL 90° process, and 9.23 μm in Line 45° process, respectively. The corresponding cooling rates show a decreasing trend, i.e., Line 45°: 179.37 k/s, CL 90°: 161.55 k/s and Line 90°: 69.92 k/s, which are calculated by Eqs 1 and 2 and they are much higher than the cooling rate of ordinary casting process (Ref 22).

The deposition samples under Line 90, CL 45° and Line 45° exhibit morphological difference due to their corresponding deposition direction and thermal cycle. Other than the depo-

sition morphological difference, the microstructure appeared to possess recrystallization in the processed material. To further elucidate the microstructural changes occurring in the inter-layer and inner-layer regions during the WAAM-CMT deposition process, electron backscattered diffraction (EBSD) is used to investigate the characteristics of microstructural features. As observed from the (100) pole figures in Fig. 6, it shows the grains appearing equiaxed along inter-layer regions are elongated in the adjacent inner-layer regions (Fig. 6a, d, h), and dynamic recrystallization (DRX) with various degree occurs in all the deposited samples. Figure 6(g) and (i) shows the overall average grain size of total regions are fine in the samples with Line 45° deposition strategy, while they are slightly big in samples with Line 90° deposition strategy. The value of cooling rates shown in Fig. 3 suggests that the diverse thermal cycle is attributed to the different deposition strategies. Fine grains are produced as a consequence of rather high cooling rates. Further, the amount of fine grains increased with increasing cooling rates and the disorder degree of the grains enhanced, which reveals that DRX occurs during the manufacturing thermal cycle, and new grains nucleation and growth process occurs. The distribution and number fraction of the DRXed (in blue), sub-structured (in yellow) and deformed (in

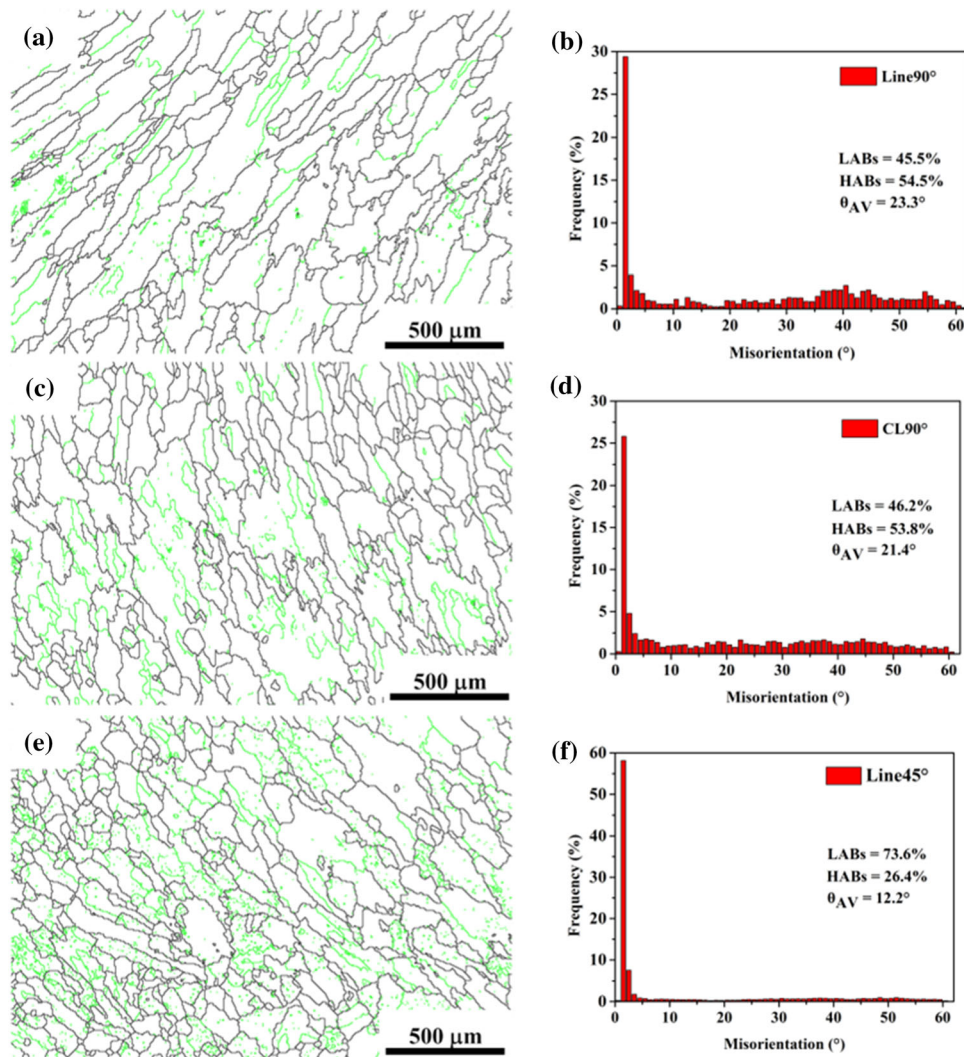


Fig. 7 Representation of HABs and LABs in the WAAM-CMT Al-5Si alloys: (a, b) Line 90°, (c, d) CL 90°, (e, f) Line 45°

red) grains are given in Fig. 6b, e, h. When the cooling rate is 69.92 k/s in Line 90° process, the sample has sufficient time for recovery and recrystallization, and the ratio of DRXed grains up to 71%. Nonetheless, comparing to Line 90° process, a heavy cooling rate causes many grains to not proceed to the recrystallization in time, thus resulting in an increase in sub-structured grains at the cooling rate of 179.37 k/s in Line 45° process. At this cooling rate (179.37 k/s), the samples exhibit the largest proportion of sub-structured grains (yellow color accounting for 59%) and deformation (red color accounting for 1%) among the three deposition strategies, owing to the short duration at the high temperature. Furthermore, the relative frequency of the misorientation angles of all samples are shown in Fig. 7, where the green color zone is the low-angle grain boundaries (LAGB, $\theta \leq 15^\circ$), and the black lines represent the high-angle grain boundaries (HAGB, $\theta > 15^\circ$). The fraction of HABs is substantially higher than that of LABs in all samples except for Line 45° samples. The average misorientation angle of HABs slightly decreases from Line 90°, CL 90° to Line 45° samples in turn, and the fraction of LABs increase with the increasing of cooling rate. This result further proves the occurrence of partial DRX, and that the DRX fraction decreases with increasing cooling rate during the WAAM-CMT process.

3.4 Micro-hardness Distribution

The micro-hardness distribution of the WAAM-CMT samples under different processing states is shown in Fig. 8. The test is conducted along the path represented by the dashed line in the inset. Along the mid-width line of the samples, the average micro-hardness value is 55.2 Hv in Line 45° process, 50.4 Hv in the CL90° process and 48.9 Hv in Line 90° process. In comparison to the average micro-hardness value of Line 90° sample along the mid-height line, the value is increased by 14.1% when using Line 45° deposition strategies. It can be concluded that varying the deposition strategy can significantly influence the micro-hardness of WAAM-CMT Al-5Si alloy. Fig. 8a shows along the mid-width direction, the micro-hardness shows the fluctuation distribution, but in the mid-height direction, it shows an initial decrease followed by an increase. In the locations along mid-width direction as the as-deposited condition, grain size is smaller in inter-layer regions than that in the inner-layer regions, and hence the micro-hardness is relatively higher (shown in Fig. 8a1, a2). Similarly, in the locations along mid-height direction, which closed to the base metal and the top region of samples, the micro-hardness values whether in inter-layer or inner-layer regions are higher owing to the formation of finer grain size (shown in Fig. 8b1,

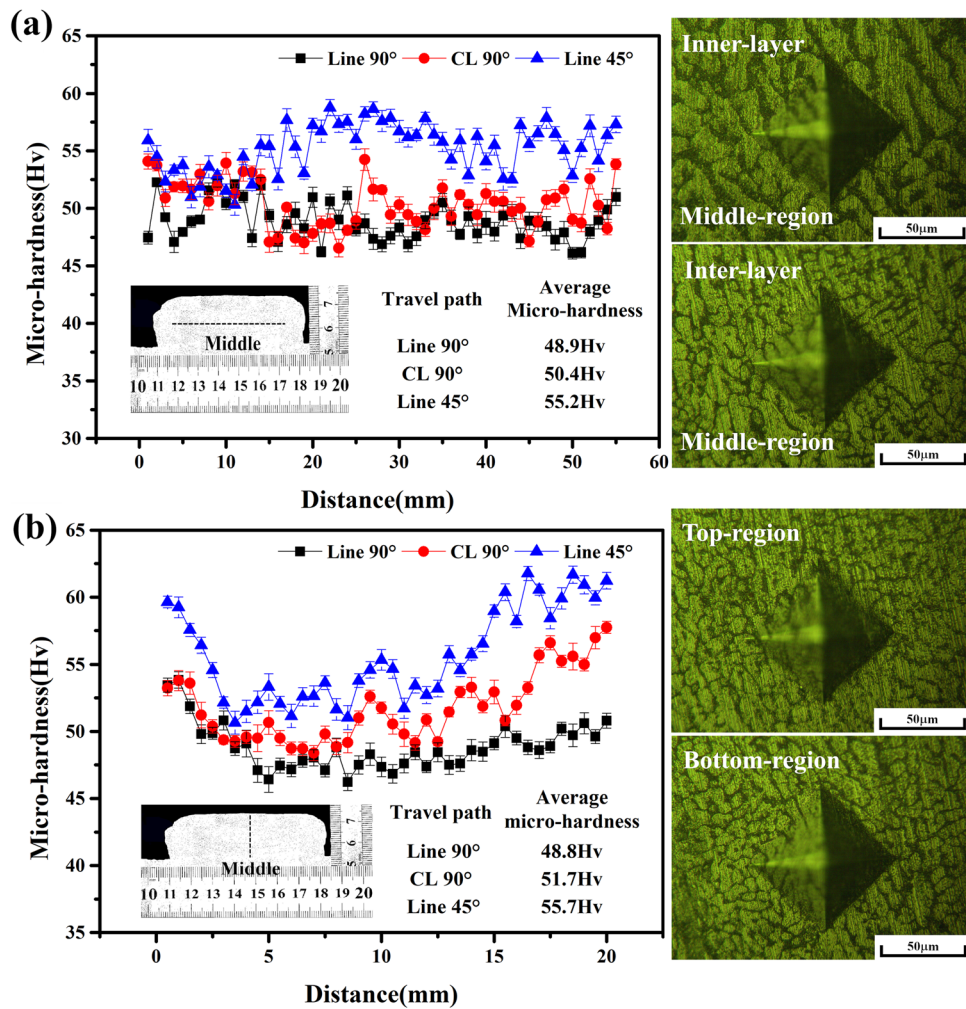


Fig. 8 The micro-hardness distribution of WAAM-CMT Al-5Si alloys: (a) along the mid-width direction: images of Line 45° micro-hardness in inner-layer (a₁) and inter-layer (a₂) regions, (b) along the mid-height direction: images of Line 45° micro-hardness in top (b₁) and bottom (b₂) regions

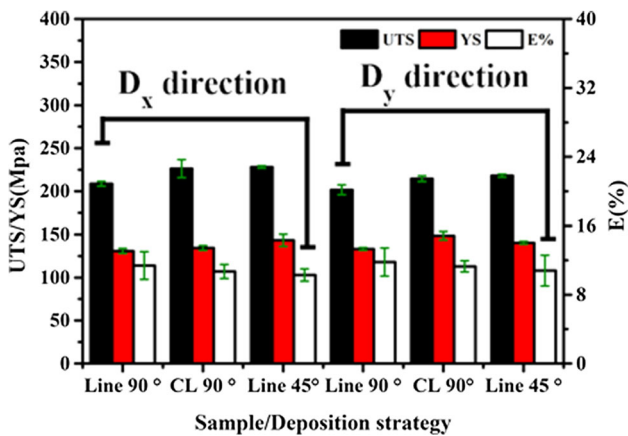


Fig. 9 The tensile properties of WAAM-CMT Al-5Si alloys under room temperature.

b₂) due to relatively fast cooling rate and lower thermal accumulation when compared to the middle region. While the presence of pores results in lower micro-hardness values, fine grain size increases the values, especially in the inter-layer region.

3.5 Tensile Properties

Considering the observations from microstructural studies, it can be seen that the three deposition strategies with corresponding cooling rates resulted in the differences of Si morphology, microstructure features and show variation in the micro-hardness values. In addition, research shows that the increased presence of (111) α -Al phase (Ref 23), low-angle grain boundaries, sub-structured grains (Ref 24, 25) and mostly fibrous morphology Si phase (Ref 26) in extremely higher cooling rate processes, contribute to the mechanical properties enhancement of the WAAM-CMT samples.

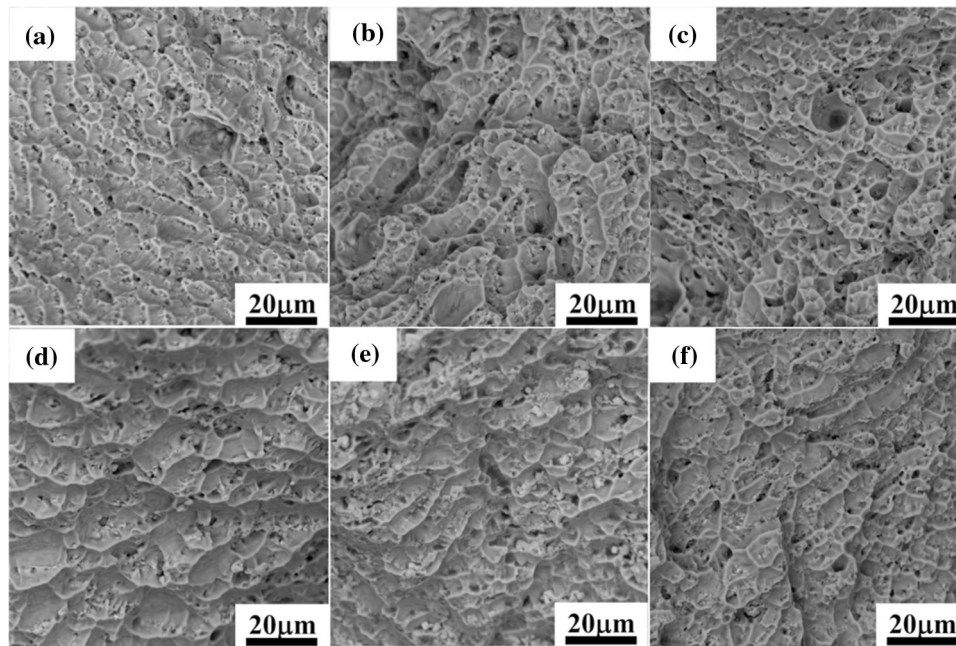


Fig. 10 Fracture surface images of WAAM-CMT Al-5Si alloys along with D_x (a, b, c) and D_y (d, e, f) directions: (a, d) Line 90° , (b, e) CL 90° , (c, f) Line 45°

Figure 9 summarizes the tensile test results and the mechanical properties (ultimate tensile strength-UTS, yield strength-YS and elongation-EL) of the samples with the tested direction of D_x and D_y . Compared to the Line 90° counterparts (UTS: ~ 205.2 MPa, YS: ~ 132.1 MPa, EL: $\sim 11.6\%$), Line 45° samples show excellent strength but less ductility (UTS: ~ 223.2 MPa, YS: ~ 141.8 MPa, EL: $\sim 10.6\%$) owing to their fine grains and microstructures caused by the faster cooling rate. Moreover, relatively higher UTS, yield strength YS and lower EL are observed along the D_x direction in these samples comparing to D_y direction. Figure 10 shows the tensile fracture surfaces of WAAM-CMT samples. In correlation with the high elongation values of WAAM-CMT samples shown in Fig. 9, the fractographic observation of the tensile samples reveals that the microscopic fracture features are all dominated by dimples because of ductile fracture mode. The average EL values in the Line 90° process, CL 90° process, and Line 45° process are 11.6, 11, and 10.6%, respectively. Also, some large second-phase particles (Al_6Si) are embedded in the dimples, and more pores are distributed on the fracture surface as observed in the D_y direction (Fig. 10d, e, f, respectively).

Due to the ease of formation and propagation of a crack, especially when the samples contain lots of pores in inter-layer regions, resulting in the fracture occur in the samples tested by tensile machine. Figure 11, 12 shows the optical microscope (OM) and SEM images of the tensile-fractured surfaces of the Al-5Si alloy parts using a Line 45° deposition strategy along the D_x and D_y direction. The results indicate that in the inner-layer regions, fracture occurs along the dendritic cell boundaries, in a transgranular manner, while for that in the inter-layer regions, the final fracture tends to occur along the grain boundaries. Both the samples along with the D_x and D_y direction show mixed-mode fracture features that consisting of

intergranular and transgranular. Transgranular fracture is found to be the main fracture mode in the samples, with a ratio of 85%. Additionally, voids, pores, and cracks are observed on the fracture surface of the samples. As shown in Fig. 11(a), (c), and (f), although pores and micro-cracks appear in the samples, more number of pores and larger pores and micro-cracks are observed in inter-layer regions compared to the inner-layer regions, indicating that fracture is more likely to occur in this region. Further, as the micro-cracks penetrate the pores in sequence, a continuous fracture path is generated, and a large number of deviating fractures appear along the micro-cracks in the regions. At the same time, as seen in Fig. 12(d) and (e), transgranular fracture and intergranular fracture appear in the inter-layer fracture area. As there is no variation in the elemental composition between them, it further confirms that the mixed-mode of intergranular fracture and transgranular fracture is not clearly defined by regions. While the inner-layer region is dominated by transgranular fracture, the inter-layer region is dominated by intergranular fracture.

4. Conclusions

In the current work, the effect of the deposition strategy on phase formation, microstructure and mechanical properties of Al-5Si alloy samples fabricated by WAAM-CMT have been investigated. The key results are drawn as follows:

1. All samples exhibit (1) recrystallization during the deposition process, (2) smaller equiaxed grains in inter-layer regions and (3) mostly columnar/columnar dendritic grains in inner-layer regions, along the building direction. The Line 45° sample has a smaller grain size, a larger

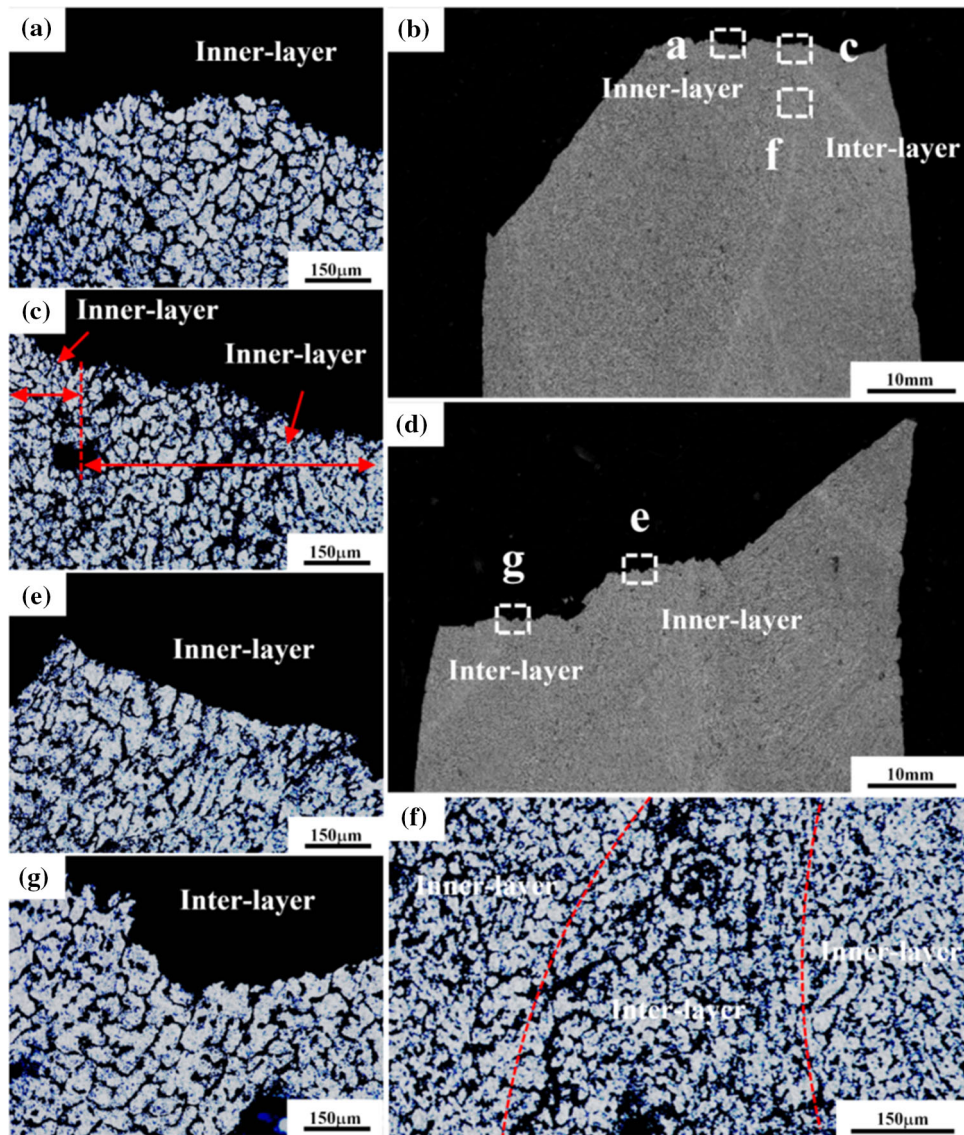


Fig. 11 Fracture sub-surfaces of D_x (a, b, c, f) and D_y (d, e, g) directions for Line 45° samples

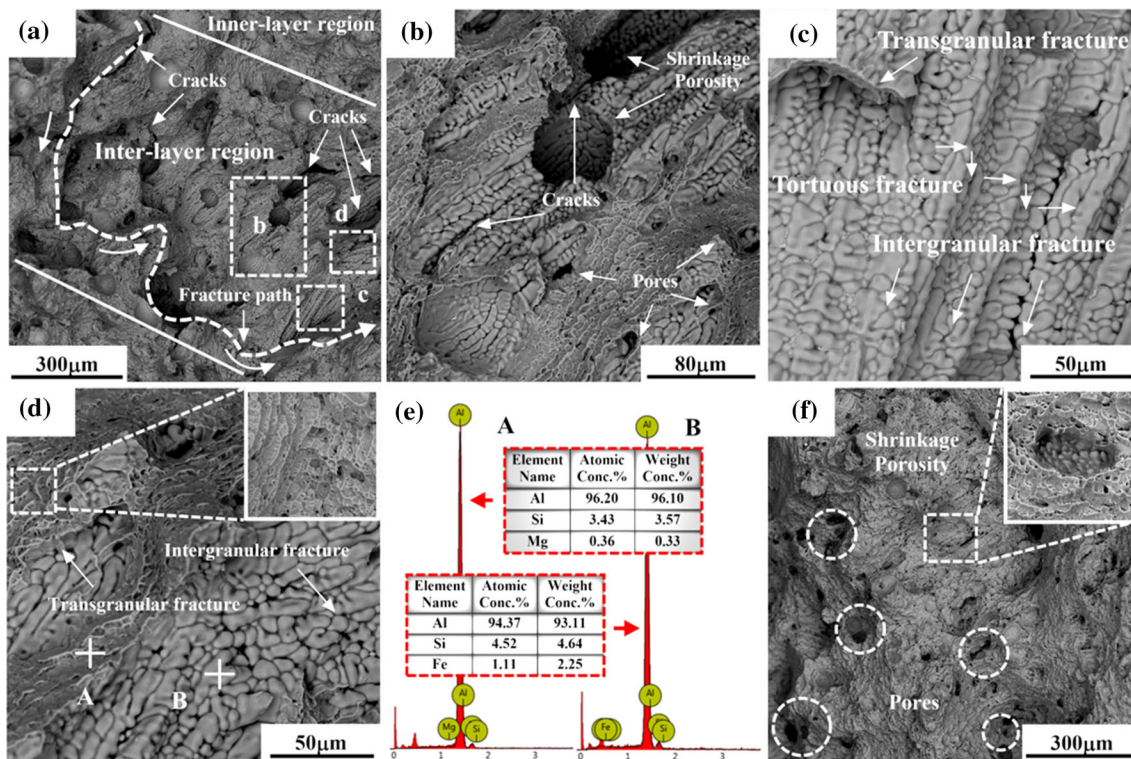


Fig. 12 The fracture analysis of Line 45° samples in inter-layer regions

number of low-angle grain boundaries and fibrous Si-morphology when compared to the Line 90° samples, whereas the CL 90° sample shows intermediate microstructural features.

- The comparably better plasticity but poorer micro-hardness and strength of Line 90° sample among all samples are attributed to the (1) coarser microstructure within grains, (2) weaker (111) orientation Al phase, (3) more high-angle grain boundaries, (4) larger columnar/columnar dendritic grains with needle-like or rod-like shape Si phases that are distributed uniformly, together brought forth by the heat treatment of subsequent deposition.
- For three deposition strategies of Line 90°, CL 90° and Line 45°, the tensile fracture initiate in the interlayer region, and micro-crack coalescence is favored due to the pores and cracked Si phase that appears in these regions. Eventually, the fracture at the inner-layer region is dominated by transgranular mode, while the inter-layer region is governed by intergranular fracture.

Acknowledgment

This work is supported by the National Natural Science Foundation of China (Grant No. 51975419) and the China Scholarship Council.

References

- T. Dursun and C. Soutis, Recent Developments in Advanced Aircraft Aluminium Alloys, *Mater. Des.*, 2014, **56**, p 862–871

- V. Sankar and S. Muthu, Investigation of Microstructure and Mechanical Behavior of AlSi7Mg, *J. Appl. Sci.*, 2014, **14**, p 811–816
- F. Trevisan, F. Calignano, M. Lorusso, J. Pakkanen, A. Aversa, E.P. Ambrosio, M. Lombardi, P. Fino and D. Manfredi, On the Selective Laser Melting (SLM) of the AlSi10Mg Alloys Process, Microstructure, and Mechanical Properties, *Material*, 2017, **10**, p 76
- J. Li, X. Cheng, Z. Li, X. Zong, X.H. Chen, S.Q. Zhang and H.M. Wang, Microstructures and Mechanical Properties of Laser Additive Manufactured Al-5Si-1Cu-Mg Alloy with Different Layer Thicknesses, *J. Alloys Compd.*, 2019, **789**, p 15–24
- S.W. Williams, F. Martina, A.C. Addison, J. Ding, G. Pardal and P. Colegrove, Wire+ Arc Additive Manufacturing, *Mater. Sci. Tech-lond*, 2016, **32**, p 641–647
- X.Z. Chen, C.C. Su, Y.F. Wang, A.N. Siddiquee, S. Konovalov, S. Jayalakshmi and R.A. Singh, Cold Metal Transfer (CMT) Based Wire and Arc Additive Manufacture (WAAM) System, *J. Surf. Invest. X-Ray. Synchrotron Neutron Tech.*, 2018, **12**, p 1278–1284
- Q.F. Yang, C.J. Xia, Y.Q. Deng, X.F. Li and H.W. Wang, Microstructure and Mechanical Properties of AlSi7Mg0.6 Aluminum Alloy Fabricated by Wire and Arc Additive Manufacturing Based on Cold Metal Transfer WAAM-CMT, *Material*, 2019, **12**, p 2525
- A. Gomez Ortega, L. Corona Galvan, F. Deschaux-Beaume, B. Mezrag and S. Rouquette, Effect of Process Parameters on the Quality of Aluminium Alloy Al5Si Deposits in Wire and Arc Additive Manufacturing Using a Cold Metal Transfer Process, *Sci. Technol. Weld. Join.*, 2018, **23**, p 316–332
- N.O. Larrosa, W. Wang, N. Read, M.H. Loretto, C. Evans, J. Carr, U. Tradowsky, M.M. Attallah and P.J. Withers, Linking Microstructure and Processing Defects to Mechanical Properties of Selectively Laser Melted AlSi10Mg alloy, *Theor. Appl. Fract. Mech.*, 2018, **98**, p 123–133
- C.C. Zhang, H.H. Zhu, Z.H. Hu, L. Zhang and X.Y. Zeng, A Comparative Study on Single-laser and Multi-laser Selective Laser Melting AlSi10Mg: Defects, Microstructure and Mechanical Properties, *Mater. Sci. Eng. A*, 2019, **746**, p 416–423
- X. Liu, C.C. Zhao, X. Zhou, Z.J. Shen and W. Liu, Microstructure of Selective Laser Melted AlSi10Mg alloy, *Mater. Des.*, 2019, **168**, p 107677

12. T. Kimura and T. Nakamoto, Microstructures and Mechanical Properties of A356 (AlSi7Mg0.3) Aluminum Alloy Fabricated by Selective Laser Melting, *Mater. Des.*, 2016, **89**, p 1294–1301
13. J. Guan, Y. Jiang, X. Zhang, X.W. Zhang and X.Y. Chong, Microstructural Evolution and EBSD Analysis of AlSi10Mg Alloy Fabricated by Selective Laser Remelting, *Mater. Charact.*, 2020, **12**, p 110079
14. K.G. Prashanth, S. Scudino and J. Eckert, Defining the Tensile Properties of Al-12Si Parts Produced by Selective Laser Melting, *Acta Mater.*, 2017, **126**, p 25–35
15. A.S. Haselhuhn, M.W. Buhr, B. Wijnen, P.G. Sanders and J.M. Pearce, Structure-property Relationships of Common Aluminum Weld Alloys Utilized as Feedstock for GMAW-Based 3-D Metal Printing, *Mater. Sci. Eng. A*, 2016, **673**, p 511–523
16. H.J. Wang, W.H. Jiang, J.H. Ouyang and R. Kovacevic, Rapid Prototyping of 4043 Al-Alloy Parts by VP-GTAW, *J. Mater. Process. Tech.*, 2004, **148**, p 93–102
17. Z. Qi, B. Qi, B.Q. Cong and R. Zhang, Microstructure and Mechanical Properties of Wire+ Arc Additively Manufactured Al-Mg-Si Aluminum Alloy, *Mater. Lett.*, 2018, **233**, p 348–350
18. L. Thijs, K. Kempen, J. Kruth and J.V. Humbeeck, Fine-structured Aluminium Products with Controllable Texture by Selective Laser Melting of Pre-alloyed AlSi10Mg Powder, *Acta Mater.*, 2013, **61**, p 1809–1819
19. T. DebRoy, H.L. Wei, J.S. Zuback, T. Mukherjee, J.W. Elmer, J.O. Milewski, A.M. Beese, A. Wilson-Heid, A. De and W. Zhang, Additive Manufacturing of Metallic Components—Process, *Structure and Properties. Prog. Mater. Sci.*, 2018, **92**, p 112–224
20. H.S. Kang, W.Y. Yoon, K.H. Kim, M.H. Kim and Y.P. Yoon, Microstructure Selections in the Undercooled Hypereutectic Al–Si Alloys, *Mater. Sci. Eng. A*, 2005, **404**, p 117–123
21. B. Jiang, Z.S. Ji, M.L. Hu, H.Y. Xu and S. Xu, A Novel Modifier on Eutectic Si and Mechanical Properties of Al-Si Alloy, *Mater. Lett.*, 2019, **239**, p 13–16
22. Q.F. Yang, C.J. Xia, Y.Q. Deng, X.F. Li and H.W. Wang, Microstructure and Mechanical Properties of AlSi7Mg0.6 Aluminum Alloy Fabricated by Wire and Arc Additive Manufacturing Based on Cold Metal Transfer (WAAM-CMT), *Material*, 2019, **12**, p 2525
23. R. Rashid, S.H. Masood, D. Ruan, S. Palanisamy, R.A. Rahman Rashid, J. Elambasseril and M. Brandt, Effect of Energy Per Layer on the Anisotropy of Selective Laser Melted AlSi12 Aluminium Alloy, *Addit. Manuf.*, 2018, **22**, p 426–439
24. X.Y. Li, W.J. Xia, H.G. Yan, J.H. Chen, B. Su, M. Song, Z.Z. Li and Y.L. Li, Dynamic Recrystallization Behaviors of High Mg Alloyed Al-Mg Alloy During High Strain Rate, *Mater. Sci. Eng. A*, 2019, **753**, p 59–69
25. G.J. Mao, R. Cao, C. Cayron, X.L. Mao, R. Logé and J.H. Chen, Effect of Cooling Conditions on Microstructures and Mechanical Behaviors of Reheated Low-Carbon Weld metals, *Mater. Sci. Eng. A*, 2019, **744**, p 671–681
26. Y.Q. Zhang, Y. Chen, Y.B. Cao, H.B. Qi and S.P. Yang, Microstructure and Mechanical Properties of Al-12Si Alloys Fabricated by Ultrasonic-Assisted Laser Metal Deposition, *Material*, 2020, **13**, p 126

Publisher's Note Springer Nature remains neutral with regard to jurisdictional claims in published maps and institutional affiliations.